

## Article

# The Influence of the Calcination Time on Synthesis of Nanomaterials with Small Size, High Crystalline Nature and Photocatalytic Activity in the TiO<sub>2</sub> Nanoparticles Calcined at 500 °C

Zahrah Alhalili and Moez Smiri \* 

Department of Chemistry, College of Sciences and Arts in Sajir, Shaqra University, Shaqra 11911, Saudi Arabia

\* Correspondence: almoez@su.edu.sa

**Abstract:** The development of new materials with diverse applications that fit well in the context of the current economy, where energy issues abound, is paramount. The goal of this study was to generate materials with high photocatalytic properties, at low cost and with less energy, and without health and ecological risks. Such materials would allow for a form of sustainable development that respects nature. This study investigated the influence of calcination time on titanium dioxide nanoparticles (TiO<sub>2</sub> NPs) produced by green synthesis using *Aloe vera* leaf extract under a constant temperature of 500 °C. The interaction between synthesis conditions like calcination time and the size of nanoparticles produced in relation to changes in photocatalytic activity were analyzed and discussed. The results showed that when calcination was increased at 500 °C, the synthesis of small-diameter nanoparticles was promoted. TiO<sub>2</sub> were 23 ± 2 nm (D1) and 83 ± 5 nm (D2) after 5 h and 1 h of calcination, respectively. Moreover, the calcination duration promoted an increase in crystalline nature. In the same way, the level of reduction of azo dye Remazol Red Brilliant F3B (RR180) increased when calcination time increased, and therefore, changed the optic and photo-catalytic properties of the TiO<sub>2</sub> nanomaterial. In addition, TiO<sub>2</sub> nanopowders (size 23 ± 2 nm) had the higher efficiency in photodegradation (100%) of dye RR180 under visible light irradiation for 60 min for up to one hour duration, but TiO<sub>2</sub> NPs (83 ± 5 nm) had the higher efficiency (100%) for up to two hours duration.

**Keywords:** *Aloe vera*; green synthesis; photocatalytic degradation



**Citation:** Alhalili, Z.; Smiri, M. The Influence of the Calcination Time on Synthesis of Nanomaterials with Small Size, High Crystalline Nature and Photocatalytic Activity in the TiO<sub>2</sub> Nanoparticles Calcined at 500 °C. *Crystals* **2022**, *12*, 1629. <https://doi.org/10.3390/cryst12111629>

Academic Editors: Sibow Wang, Guangzhao Wang and Tingwei Zhou

Received: 31 October 2022

Accepted: 10 November 2022

Published: 13 November 2022

**Publisher's Note:** MDPI stays neutral with regard to jurisdictional claims in published maps and institutional affiliations.



**Copyright:** © 2022 by the authors. Licensee MDPI, Basel, Switzerland. This article is an open access article distributed under the terms and conditions of the Creative Commons Attribution (CC BY) license (<https://creativecommons.org/licenses/by/4.0/>).

## 1. Introduction

Various new technologies have been integrated into the process of depolluting effluents. This has been achieved using filter membranes (microfiltration, ultrafiltration, nanofiltration, etc.), reverse osmosis, evaporation, electrophoresis and nanomaterial technologies [1–3]. In fact, many industrial sectors use this technology for wastewater treatment, in the textile industry, in the food industry and in the pharmaceutical sector [4,5]. The presence of compounds in sewer systems, water mains and oil installations (pipes, refrigeration circuits, storage tanks, fire protection systems, etc.) reduces economic profitability and causes environmental pollution [6–8]. The rapid development of various chemical industries, especially nanomaterials, must eliminate production problems and improve quality. The product is based on clean, safe and energy-efficient technology [9–11]. Recently, significant research efforts have been devoted to material catalytic reactors, such as nanomaterial reactor types, which are multifunctional catalytic reactors that integrate nanomaterials and chemical reactions into a single unit [12–18]. Proper design of the catalytic nanomaterial reactor improves efficiency and reduces downstream separation costs. As a result, catalytic nanomaterial reactors are an important technology in various industrial fields, including biotechnology, pharmaceuticals, petrochemicals, chemical plants, energy and environmental applications [17–23]. This process is an innovative alternative to sustainable growth that

relies on a design strategy to obtain benefits in manufacturing and processing. It depends on reducing the size of industrial equipment, reducing financial costs, energy consumption, environmental impact, increasing the efficiency of industrial facilities and safety controls. Conventional treatment methods do not provide effective removal of contaminants. For the breakdown of contaminants, photocatalytic oxidation using titanium dioxide ( $\text{TiO}_2$ ) is efficient.  $\text{TiO}_2$  is popular because it is stable, insoluble, nontoxic, corrosion-resistant and cheap.  $\text{TiO}_2$  powders, whether commercial or self-synthesized, exhibit substantial differences in structure, particle size, and electronic characteristics, all of which affect  $\text{TiO}_2$  photoactivity. Wang et al. [17] demonstrated that particle size has a significant impact on the kinetics of  $e^-/h^+$  recombination in nanocrystalline  $\text{TiO}_2$ -based catalysts. According to Jang et al. [18], when the particle size dropped and the anatase mass percentage rose, a greater degree of methylene blue breakdown by  $\text{TiO}_2$  nanoparticles was found under the irradiation of a black light.

In the photodegradation of rhodanide B, Hao [19] examined various  $\text{TiO}_2$  particles (8, 16 and 150 nm), and found that the smaller photocatalyst particles increased product yields more than the larger ones. When employing  $\text{TiO}_2$  catalysts with crystal particle or primary sizes bigger than 7 nm, Maira et al. (2000) [20], discovered that the smaller crystals had a larger surface area and demonstrated higher trichloroethylene degradation. The photoactivity appeared to diminish as particle size increased. Nevertheless, Krysa et al. [21] found that while synthesized  $\text{TiO}_2$  had a greater surface area than Degussa P25, its photoactivity was lower and did not reflect the higher surface area.

Metal oxide nanoparticles have attracted a lot of attention in a variety of disciplines, including the physical, chemical, biological, medicinal, optical, mechanical and engineering sciences, due to their large surface area. Spray-pyrolysis, sol-gel, hydrothermal synthesis, coprecipitation, and thermal breakdown have all been utilized to make  $\text{TiO}_2$  nanoparticles. Some hazardous compounds are absorbed and displayed at the surface as a result of chemical production processes, which may have adverse consequences in medical applications.

Recently, biosynthesis or green synthesis has emerged as an alternative process for NPs preparation. The benefit of plant extracts is providing a biological synthesis route of several NPs. Such synthesis routes are more environmentally friendly, cost-effective, biocompatible, safe, and give a regulated synthesis with defined size and morphology of NPs. There is no obligation to add different chemical stabilizers, since the extract is combined with a salt solution as the precursor, and the plant extract acts as a reducing and stabilizing agent for the synthesis of NPs [24]. In this study, an eco-friendly and rapid method for the synthesis of  $\text{TiO}_2$  NPs was described. To the best of our knowledge, this is the first time that a study has attempted to exploit the *Aloe vera* leaves extract as a reducing agent in the green synthesis of  $\text{TiO}_2$  NPs. The aim of this work was to improve the effects of different sizes of  $\text{TiO}_2$  biosynthesized particles on the photoactivity of a commercial textile dye, and the particle size changes were tracked over time. This study addressed the link between the photooxidation rate of azo dye and the average particle size of nanoparticle aggregates. The study looked to synthesize  $\text{TiO}_2$  NPs by green synthesis and studied the possibility of modifying the properties of the nanoparticles by changing the plant extract properties and synthesis conditions.

## 2. Materials and Methods

### 2.1. Materials

This study investigated the synthesis of  $\text{TiO}_2$  using *Aloe vera* as the model crop. *Aloe vera* plants are among the most important crops, and they are naturally grown anywhere in the world. They are easily cultured and maintained in laboratory conditions. Figure 1 shows the structure of RR180.

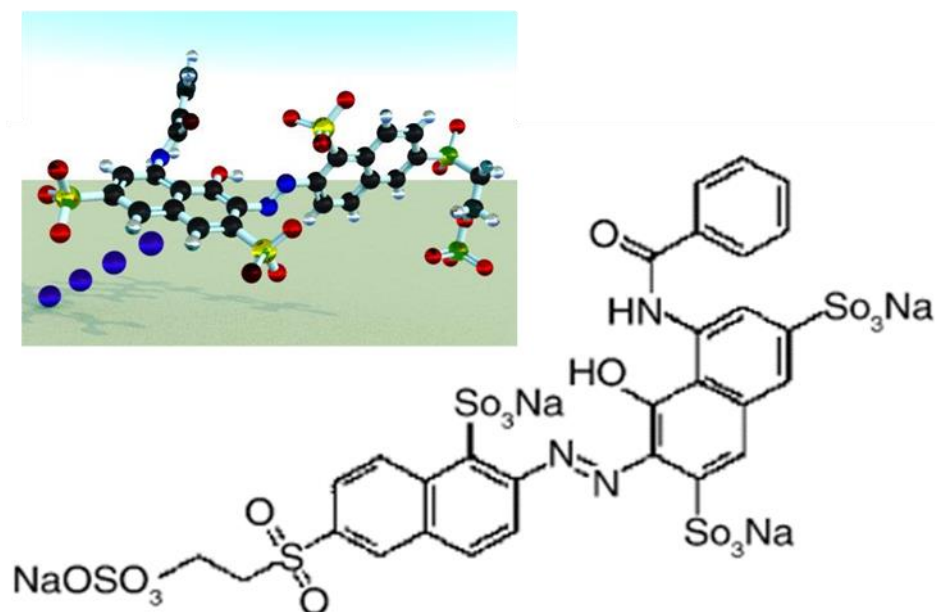


Figure 1. Remazol Brilliant Red F3B (Reactive Red 180).

## 2.2. Synthesis of TiO<sub>2</sub>

*Aloe vera* plant leaves were collected from Shaqra, Saudi Arabia. Synthesis of TiO<sub>2</sub> was performed according to Rao et al. [24].

The leaves of *Aloe vera* were separated from the plant and thoroughly washed, and then cut into small pieces. An amount of 25 g of leaves were put into 100 mL distilled water and boiled for 2 h at 90 °C. The extract was filtered using Whatman filter paper. The filtrate was stored for the synthesis of nanoparticles.

To synthesize the TiO<sub>2</sub> nanoparticles, 1.0 N of Titanium Chloride (TiCl<sub>4</sub>) (purity ≥ 99.0%, CAS number: 7550-45-0) was dissolved in 100 mL of Millipore water. Leaf extract was added dropwise under constant stirring to achieve a solution with a pH of 7. The mixture was subjected to continuous stirring for 4 h. In this process, nanoparticles were formed, and afterwards separated using Whatman filter paper and repeatedly washed with water to remove any byproducts. The nanoparticles were dried at 100 °C overnight and calcined in a muffle furnace at 500 °C without any special atmosphere for 5 and 1 h for samples with the designations D1 and D2, respectively. The calcination took place for 5 h and 1 h.

## 2.3. Characterization of TiO<sub>2</sub> Analysis

To describe their structural and textural characteristics, the TiO<sub>2</sub> nanoparticle powders underwent a variety of procedures for characterization. The crystalline phase was analyzed by X-ray. X-ray powder diffraction data (XRD) were collected on an X'Pert Pro Panalytical diffractometer with CuKα radiation ( $\lambda = 0.15406$  nm) and graphite monochromatic. The XRD measurements were performed using a phase scanning method (range from 10 to 85); the scanning rate was 0.02 s<sup>-1</sup> and the step time was one second. The infrared spectrum was registered by a Perkin-Elmer (FTIR 2000) spectrometer using KBr pellets in the region of 4000–400 cm<sup>-1</sup>. UV-vis diffuse reflectance spectroscopy (DRS) spectra were reported using UV spectrophotometers with a wavelength range of 200–1400 nm. The photoluminescence (PL) emission spectra were recorded using a Perkin-Elmer spectrophotometer (LS 55) with a Xenon lamp. The sample excitation was achieved at 325 nm at room temperature, and the emission was examined between 400 and 700 nm. Using scanning electron microscopy (SEM), morphology was examined (Philips XL30 SFEG). The TiO<sub>2</sub> tablet was 13 mm in diameter and 0.6 mm in thickness, and it was made by placing approximately 200 mg of TiO<sub>2</sub> powder under a pressure of 12 MPa for 1 min in a metal cylinder. The microstructure and phase composition of the TiO<sub>2</sub> samples were analyzed using the method described by Zhong et al. [25].

#### 2.4. Photocatalytic Runs

The photocatalytic activity of TiO<sub>2</sub> NPs was determined [26,27]. A model azo dye, Remazol Brilliant Red F3B (Reactive Red 180) (RR180), was used without further purification (CAS Number: 98114-32-0). Before initialization of the experiment, the powder was sonicated for 30 min to distribute and enhance the adsorption level. After 30 min, an ultrasonic horn was used for further distribution of the powder for 15 min to obtain a homogeneous solution. This two-step distribution process was enough to maintain the adsorption-desorption level and a homogeneous dye solution with uniformly distributed TiO<sub>2</sub> particles. In each photocatalytic degradation process, a fresh batch of 500 mL aqueous solution of RR180 azo dye was prepared by diluting the dye in the deionized water to achieve a concentration of 50 mg L<sup>-1</sup>. The degradation reactions were carried out in a laboratory-scale photo-reactor capable of housing UVA-emitting wavelength lamps. The light intensities of the lamps were measured by a UV light meter at 3.5 mWcm<sup>-2</sup> for UVA (Lutron UVA-365 sensor, Taipei, Taiwan) within the reactor. Cooled air was blown into the batch and the reactor in order to feed and accelerate the reactions, and to keep the reactor temperature around 25 °C (see Figure 2). The temperature and the pH of the solution were monitored during the reactions by a portable pH meter (VWRMulti 340i, Weilheim, Germany). Catalyst concentrations were adjusted to 0.5 g L<sup>-1</sup> in order to explore the activity of the nanopowder. The suspension was sonicated for 30 min in an ultrasonic bath and 15 min under an ultrasonic horn to homogeneously maintain the powder distribution. During the experiments, a sample was taken from the solution to detect concentration changes at 15 min intervals. Each sample was centrifuged at 6000 rpm by centrifugation; then, the absorbance of the sample was detected by using a UV-Vis spectrophotometer (Hach-Lange DR3800, Loveland, CO, USA) at 540 nm maxima. The absorbance values were converted to concentration values by using the Beer-Lambert's law. Final degradation rate values were evaluated by the formula below:

$$D(\%) = \frac{C_0 - C}{C_0} \times 100 \quad (1)$$

where  $C_0$  is the concentration of RR180 at equilibrium established under dark conditions and  $C$  is the concentrations of the dye solution taken at different irradiation time intervals.

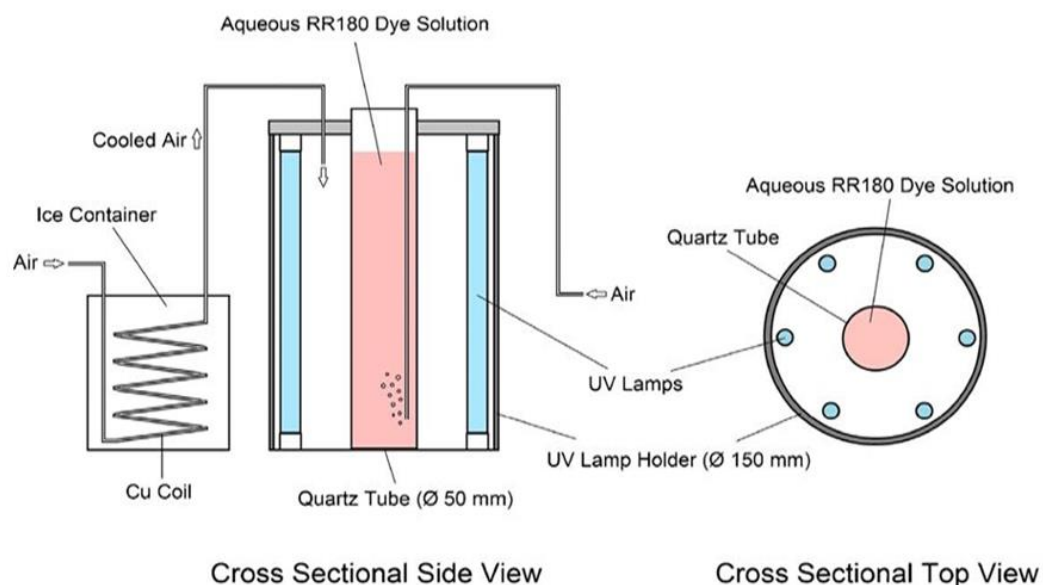


Figure 2. The schematic diagram of the photocatalytic reactor.

### 3. Results and Discussion

#### 3.1. Characterization Results

Spectra corresponding to TiO<sub>2</sub> (1 h) and TiO<sub>2</sub> (5 h) are shown in Figure 3. The observed XRD peaks are in good agreement with the standard JCPDS file (84–1285), which confirms an anatase structure at all peaks. Favored growth is located along the crystal plane (101). No excess peaks were observed, suggesting that nanocrystals TiO<sub>2</sub> were established at 500 °C. The average particle size (*D*) of the samples as prepared was determined using the Debye—Scherrer formula, as shown by Equation (2):

$$D = k \times \lambda / \beta \cos\theta \quad (2)$$

where *D* is crystallite size in nm,  $\lambda$  is the wavelength (1.5406 Å) of the Cu K-alpha X-ray radiation used,  $\theta$  is the Bragg angle and  $\beta$  is the full-width at half-maximum (FWHM) which corresponds to the most popular peak (101) expressed in radians.

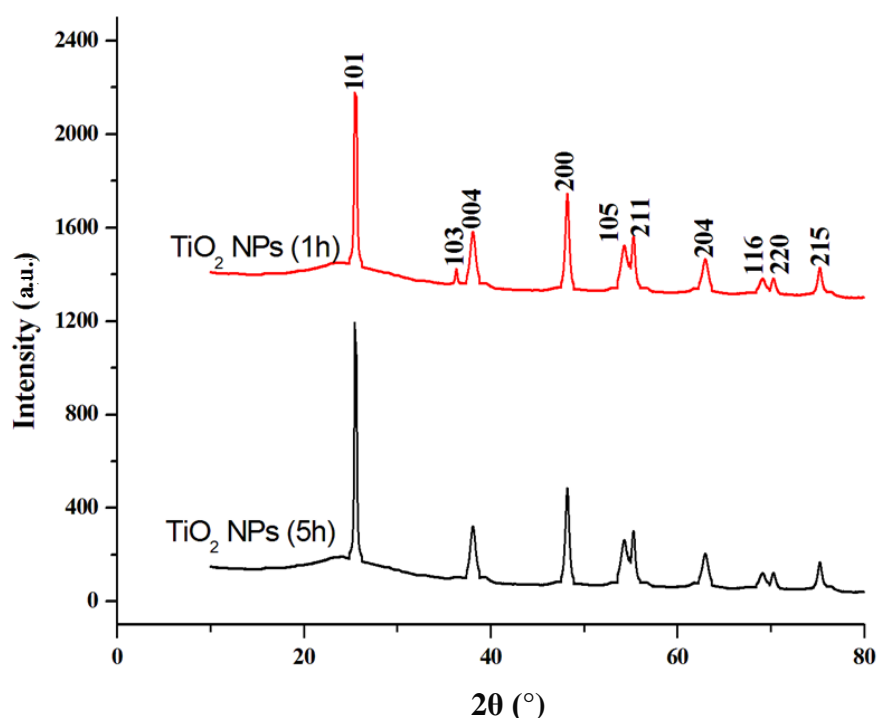


**Figure 3.** X-ray diffraction (XRD) of TiO<sub>2</sub> nanoparticles (NPs).

The average crystallite size of the TiO<sub>2</sub> nanoparticles was considerably decreased from  $83 \pm 15$  nm to  $23 \pm 1.6$  nm when the duration of calcination increased from 1 h to 5 h, respectively. The decrease in particle size with a duration of 5 h can be attributed to higher precipitation intensity. The average crystal size of TiO<sub>2</sub> NPs significantly decreased from  $83 \pm 5$  nm to  $23 \pm 2$  nm when the calcination time increased from 1 h to 5 h. Plant extracts were chosen instead of chemical reactants. This provided us with a cost saving, and an environmental gain that promotes sustainable development. We varied the calcination time to see the influence of the exposure of nanoparticles to short and long durations on the structural and optical properties, as well as to see how we could obtain good-quality nanoparticles at the same time as gaining energy. The interaction between these different factors is the promoter for the best material and the right conditions of synthesis. For this reason, we chose the right synthesis conditions and selected the right materials; innovations and elements that have relevance today. The anatase titanium dioxide structure was the best photocatalyst obtained by modifying synthesis conditions, especially type of precursor, temperature and washing steps [28–35].

The structural properties of nanoparticles (shape and size) are very important data sources for the valorization of material (Figure 4). SEM images confirmed the existence of nanoparticle clusters and exhibited a sphere-filled shape. The typical manual histogram is shown in Figure 4C,D. Image J software showed the size distribution of TiO<sub>2</sub> NPs. The TiO<sub>2</sub> NPs particle size at 500 °C for one h and five h was 84 nm and 25 nm, respectively. Several factors can influence green synthesis, mostly the type of plant extract, pH and temperature. As described in this work, at a temperature of 500 °C, the increase in calcination time promoted the synthesis of small diameter nanoparticles. Temperature was an important parameter and influenced the structural and textural properties of catalysts. Calcination temperature revealed that aging time affects the size and morphology of the nanoparticles. In the literature, it has been determined that the titanate phase transforms to an anatase phase at a calcination temperature higher than 500 °C. The intensity of the rutile phase increased in the calcination temperature range from 700 to 900 °C [36]. In a study reported by Indrayana et al. [37], nanoparticle size decreased with temperature and dwelling time from 2 h to 4 h. D1 particles were smaller than D2, as shown by the results of the spectrum of photon energy. The Debye–Scherrer formula was applicable for the present work [29]. Based on these results, we can suggest that the elongation of calcination time could positively affect the structure of green synthesis TiO<sub>2</sub> NPs, but under a controlled temperature at 500 °C.

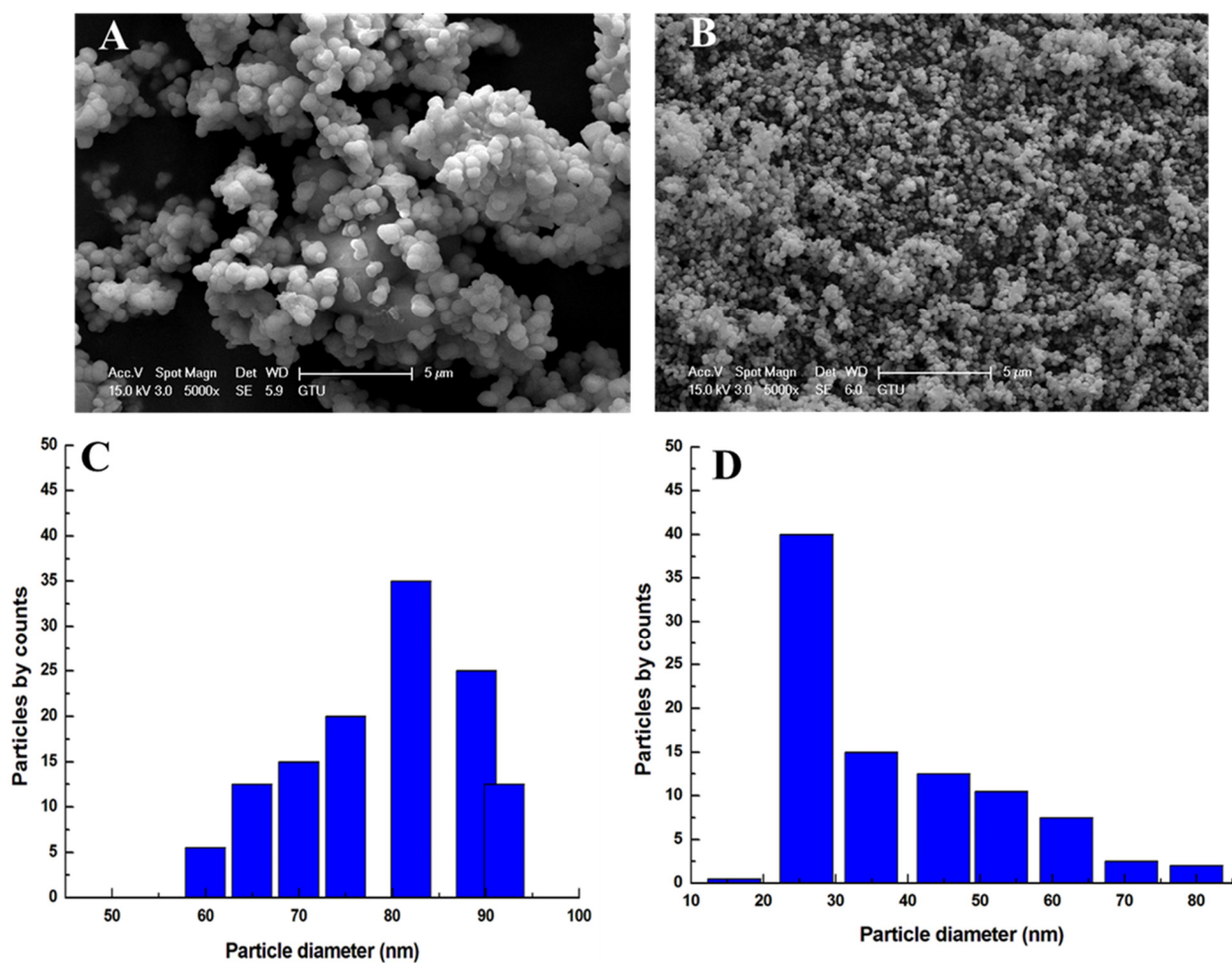


**Figure 4.** Scanning electron microscope (SEM) image of TiO<sub>2</sub> nanoparticles ((A) for TiO<sub>2</sub> NPs at 1 h, and (B) for TiO<sub>2</sub> NPs at 5 h) at ×5000 magnification and histogram of particle size distribution curve of TiO<sub>2</sub> NPs ((C) for NPs at 1 h and (D) for NPs at 5 h).

Figure 5 shows the infrared absorption range of TiO<sub>2</sub> NPs. The spectra of TiO<sub>2</sub> NPs show a strong absorption band between 800 and 450 cm<sup>-1</sup>, which is attributed to the Ti-O vibration mode. Crystalline solids are never perfect [23]. Some defects affect band profiles. In fact, in TiO<sub>2</sub> oxide, defects can come in the form of atomic vacancies or atoms in interstitial positions [28].

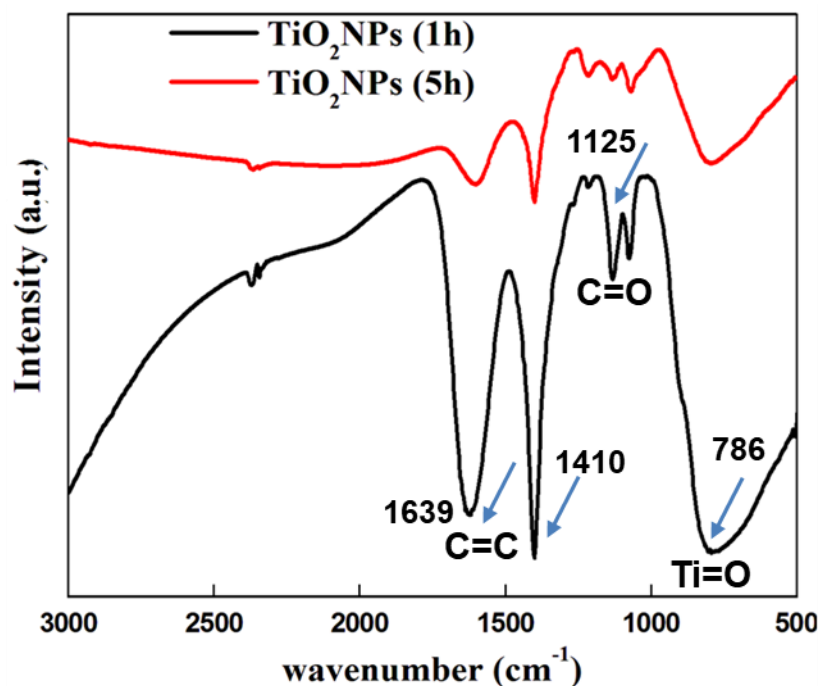


Figure 5. FTIR spectra of TiO<sub>2</sub> nanoparticles.

For this purpose, we used photoluminescence (PL) at room temperature. The photoluminescence spectra of TiO<sub>2</sub> nanospheres are shown in Figure 6. The spectrum analysis shows the presence of a series of bands located around 442, 489, 506, 532 and 570 nm. These emission bands are attributed to surface state emissions and are due to the recombination of the trapped electron-hole resulting from dangling bonds in the TiO<sub>2</sub> nanoparticles. Indeed, the band localized around 442 nm can be attributed to the transition of electrons through defect levels in the band gap, such as the oxygen gap that formed during sample preparation [38]. The emission band located around 534 nm is due to O<sup>2-</sup> vacancies.

Photoluminescence is mainly a surface phenomenon. Therefore, it was concluded that the visible luminescence band originates from oxygen vacancies associated with Ti<sup>3+</sup> in anatase TiO<sub>2</sub>. These results are in alignment with other results presented in the literature [39].

The influence of calcination time has been investigated on the optical properties of TiO<sub>2</sub> nanopowders prepared via green synthesis process. TiO<sub>2</sub> D1 and D2 are composed of a wide absorbing band, the maximum of which is in the UV zone around 344 and 302 nm, respectively (Figure 7). The single absorption band present on all the spectra is attributed to the gap transition of TiO<sub>2</sub> (interband electronic transition). The variation of the absorbance in this region is used for the gap determination. Results in Figure 8 show a straight line, which indicates that the optical transition is direct. From the graphical representations, the values of the gap energy E<sub>g</sub> determined from the absorption spectra are 3.02 and 3.19 eV for TiO<sub>2</sub> for 1 h (Figure 8A) and 5 h (Figure 8B), respectively. These values are lower than those reported in the literature; 3.27 eV for bulk TiO<sub>2</sub> [40]. After prolonged calcination, the typical TiO<sub>2</sub> band gap was likely reduced as a result of oxygen vacancies acting as electron donors in the photocatalyst's valence band, which led to the formation of additional layers (microstates) with novel electronic properties and further decreased the energy absorption gap [41].

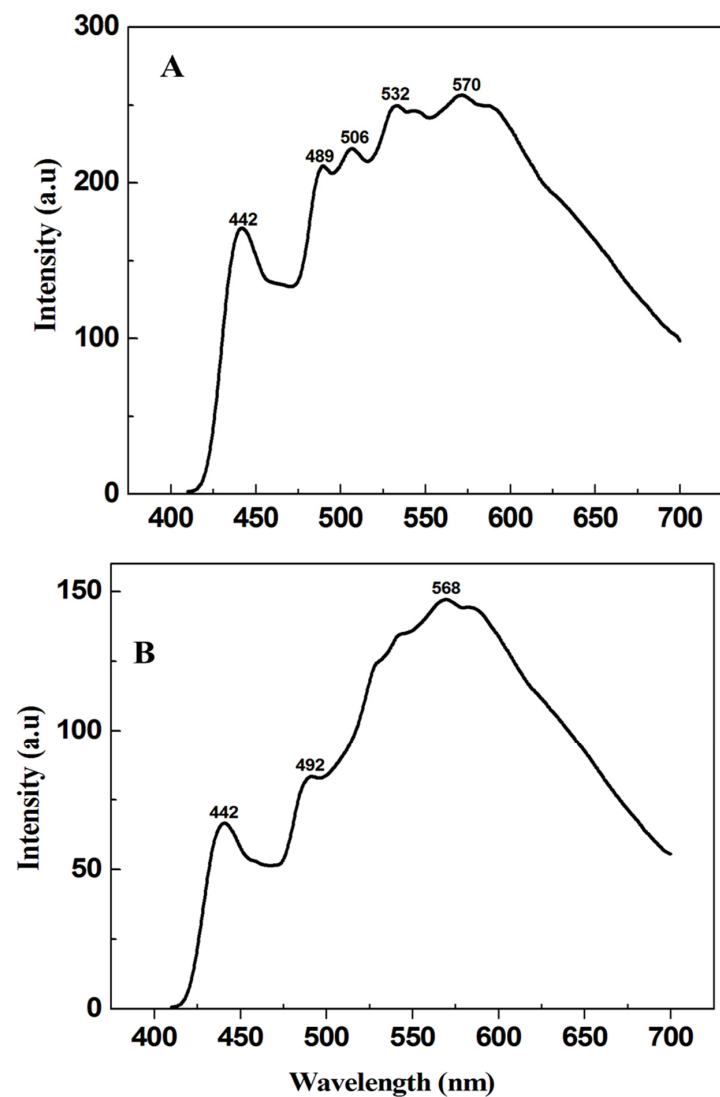


Figure 6. Photoluminescence of TiO<sub>2</sub> nanoparticles ((A) for TiO<sub>2</sub> NPs at 1 h, and (B) for TiO<sub>2</sub> NPs at 5 h).

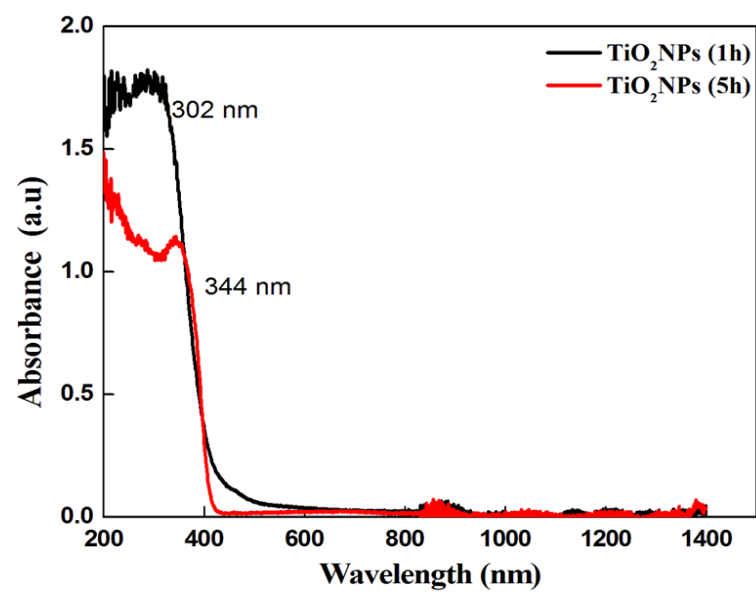
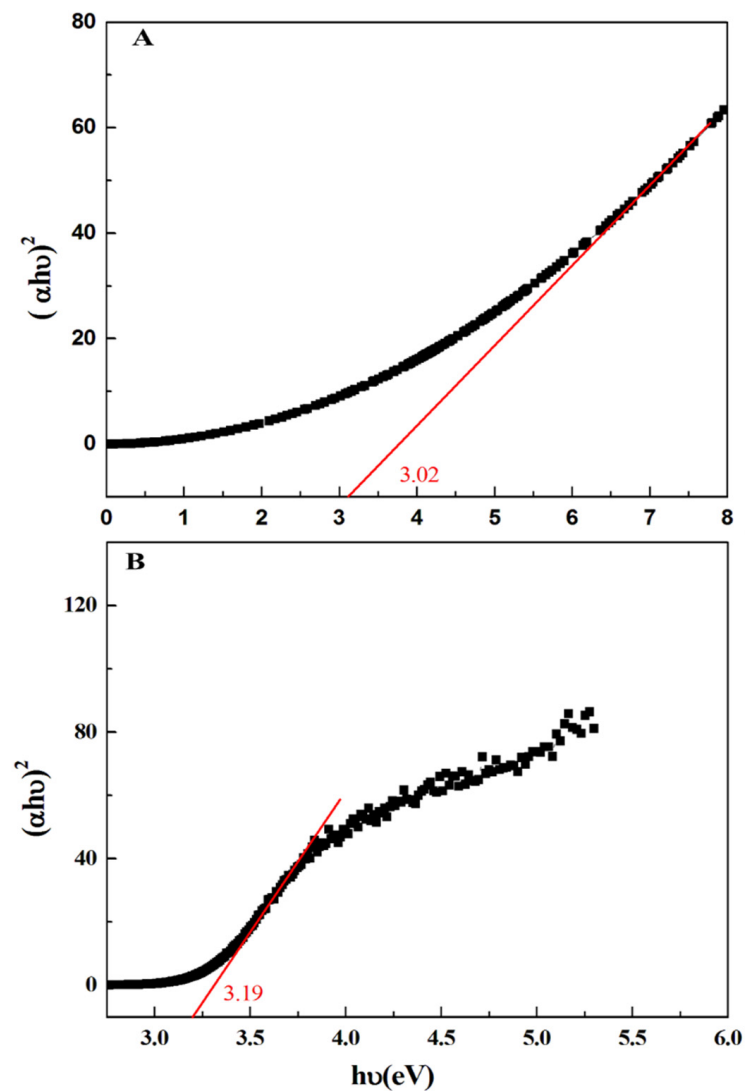


Figure 7. UV-DRS curves of TiO<sub>2</sub> nanoparticles.



**Figure 8.** Spectrum of photon energy  $(\alpha h\nu)^2$  as a function of the  $h\nu$  photon of TiO<sub>2</sub> nanoparticles (A) for TiO<sub>2</sub> NPs at 1 h, and (B) for TiO<sub>2</sub> NPs at 5 h.

### 3.2. Photocatalytic Results

The photocatalytic mechanisms of the TiO<sub>2</sub> nanoparticles irradiated with UVah light for the degradation of RR180 are presented in Figure 9. When TiO<sub>2</sub> NPs were irradiated, the •OH radical level was significantly increased. The mechanism was previously described by Jain and Vaya [35]. The •OH radicals are commonly considered to be the active species in photodegradation for the mineralization of organic dyes via photocatalysis. We used a fluorescence technique to compare the production of •OH radicals after irradiating TiO<sub>2</sub> NPs D1 and D2. Hydroxyl radicals are well-known for reacting with disodium terephthalate (DST) to produce 2-OH-DST, which emanates a strong fluorescence centered at 428 nm upon excitation at 312 nm. As can be seen in Figure 9, a significant increase in fluorescence intensity at 428 nm was observed by prolonging the irradiation time. When TiO<sub>2</sub> NPs (25 nm) were irradiated, the generation of •OH radicals significantly increased. For example, after 20 min of irradiation, TiO<sub>2</sub> NPs (25 nm) produced approximately 2.7 times more •OH radicals than TiO<sub>2</sub> NPs (83 nm) in the same experiment (Figure 10). Notably, 2-OH-DST was not produced in controlled experiments performed without light irradiation, thus confirming a photo-induced mechanism.

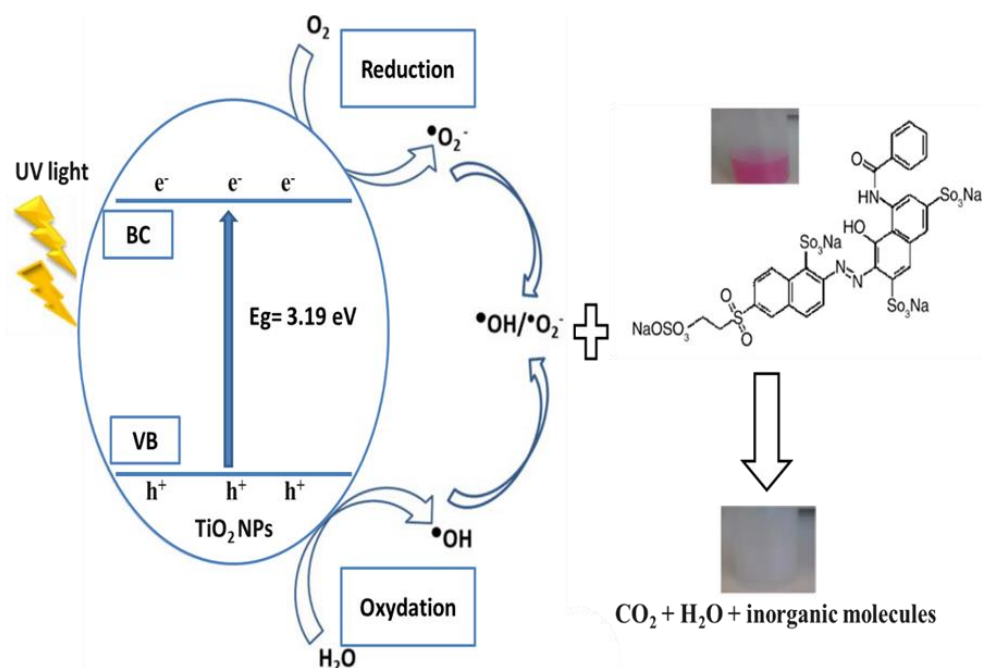


**Figure 9.** The photocatalytic mechanism of the  $\text{TiO}_2$  nanoparticles irradiated with UV light for the degradation of Remazol Brilliant Red F3B (Reactive Red 180).

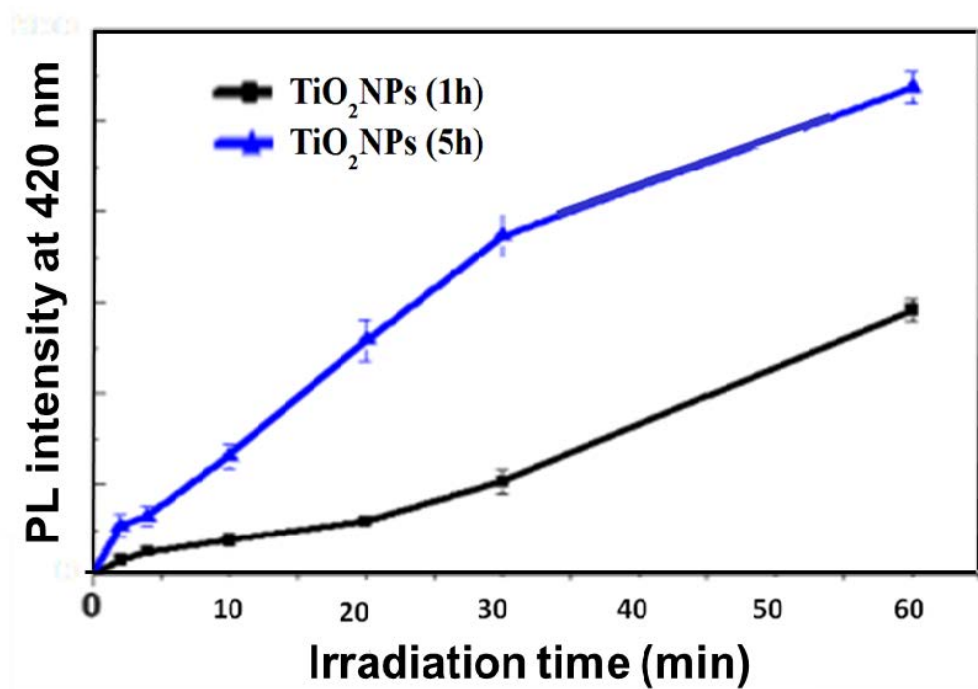


**Figure 10.** Variations of the PL intensity at 428 nm of 2-OH-DST upon irradiation of DST with  $\text{TiO}_2$  NPs (1 h) and  $\text{TiO}_2$  NPs (5 h) nanoparticles.

Photocatalytic activity of the  $\text{TiO}_2$  nanomaterials was largely dependent on material structure, and therefore, synthesis conditions. To compare the performances of the different diameters of  $\text{TiO}_2$  photocatalyst (D1 and D2) obtained after controlling calcination time under a constant temperature of  $500\text{ }^\circ\text{C}$ , photodegradation experiments on azo dye (RR180) were performed in the same photochemical reactor, with  $50\text{ mg/L}$  of azo dye (RR180), at  $T = 25\text{ }^\circ\text{C}$  and  $0.25\text{ g/L}$  of  $\text{TiO}_2$ .

The curves in Figure 11 show the results of the photodegradation of the azo dye in relation to the  $\text{TiO}_2$  irradiation time. We studied decolorization by heterogeneous photocatalysis using  $\text{TiO}_2$  as a suspended catalyst. The activity was followed by decolorization (Figure 12). The RR180 photodegradation spectra at a pH of 4.5 show a rapid decrease in RR180 absorption at 540 nm. From Figures 11 and 12A,  $\text{TiO}_2$  NPs (D1 and D2) show pronounced photocatalytic activity towards RR180 degradation. Indeed, RR180 concentration decreases with increased time of exposure to visible light. After 60 and 120 min, about 100% of the bleaching process was performed with  $\text{TiO}_2$  NPs (D1) and (D2), respectively. We observed that  $\text{TiO}_2$  NPs (D1) produced more photodegradation of RR180 compared to that of  $\text{TiO}_2$  NPs (D2). The photoreactivity of  $\text{TiO}_2$  decreased with increasing particle sizes. The rate constant for  $\text{TiO}_2$  NPs (D2) was twice that of the  $\text{TiO}_2$  NPs particles (D1) (Figure 12B). The size, the specific surface of the particles and the crystalline structure of  $\text{TiO}_2$  improved photodegradation [42–44]. However, other authors have observed an optimum size value for which photoactivity was highest [45]. The specific surface also influences the band gap energy, which defines the number of photons that can be absorbed. Therefore, for better photoactivity, it is essential to strike a compromise between the specific surface and the charge carrier dynamics [46,47]. The size effect is highly relevant for  $\text{TiO}_2$  NPs catalysis. In many cases, nanoparticles exhibit catalytic activity. The size of nanoparticles affects the mechanism of their photocatalytic activity [47–50].

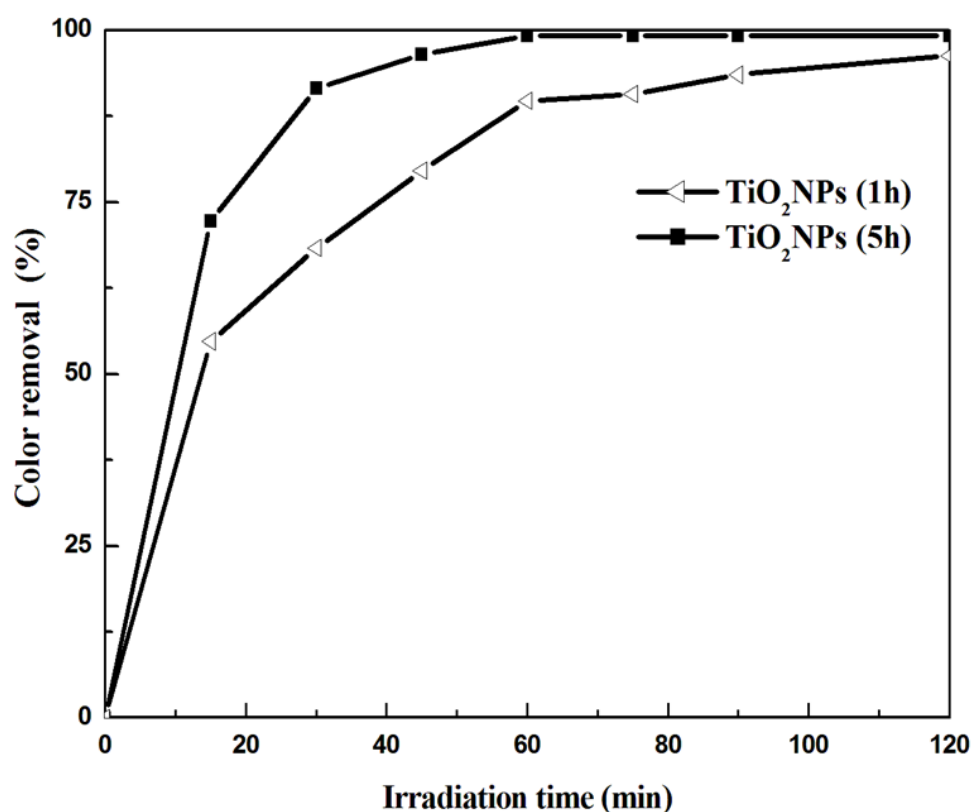
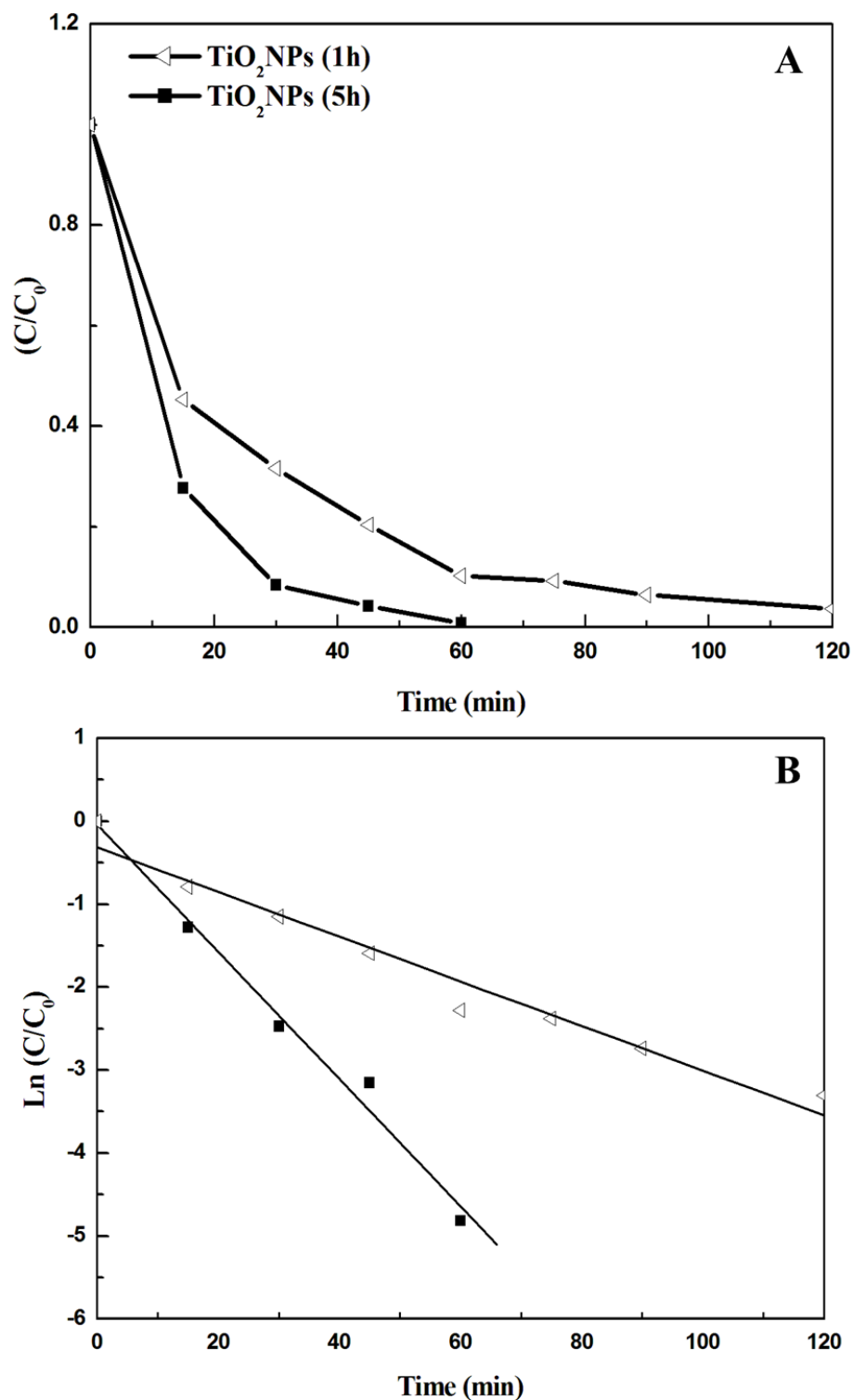


Figure 11. Photocatalytic degradation rates of  $\text{TiO}_2$  nanoparticles.

Moreover, the type of light in the photocatalysts system largely influenced photodegradation processes [51–55]. Due to better crystallinity and the removal of byproducts, the photocatalytic activity of the  $\text{TiO}_2$  NPs improved when the temperature was raised; however, it worsened above 500 °C due to the reduced surface area. These findings imply that tailoring the morphology, crystallinity, and photocatalytic activity of  $\text{TiO}_2$  NPs can be achieved by adjusting the calcination temperature [56].



**Figure 12.** Photocatalytic degradation of RR180 of TiO<sub>2</sub> nanoparticles under UV light irradiation (A) and first order linear transforms of disappearance of RR180 (B).

### 3.3. Reusability Test

Five runs of cycling photodegradation studies for the TiO<sub>2</sub> catalyst utilizing RR180 as a target substrate were carried out to assess the photocatalyst's stability. In every recycling stage of bioprepared TiO<sub>2</sub> NPs, the NPs were separated from the degraded RR180 solution by centrifugation (10,000 rpm for 5 min). Intensive washing was performed with distilled water and the particles were dried to study the recyclability of the catalyst. The results

of the RR180 dye removal efficiency as a function of the number of cycles are shown in Figure 13. The photocatalyst can be reused for up to 5 runs with a reduction efficiency of 94%, according to the findings. After each cycle, degradation efficiency gradually decreased, which is likely owing to the loss of part of the catalyst during the recycling process. These findings contribute to significant photocatalytic efficiency, photocatalyst durability and stability in the removal of RR180 dye from the solution.

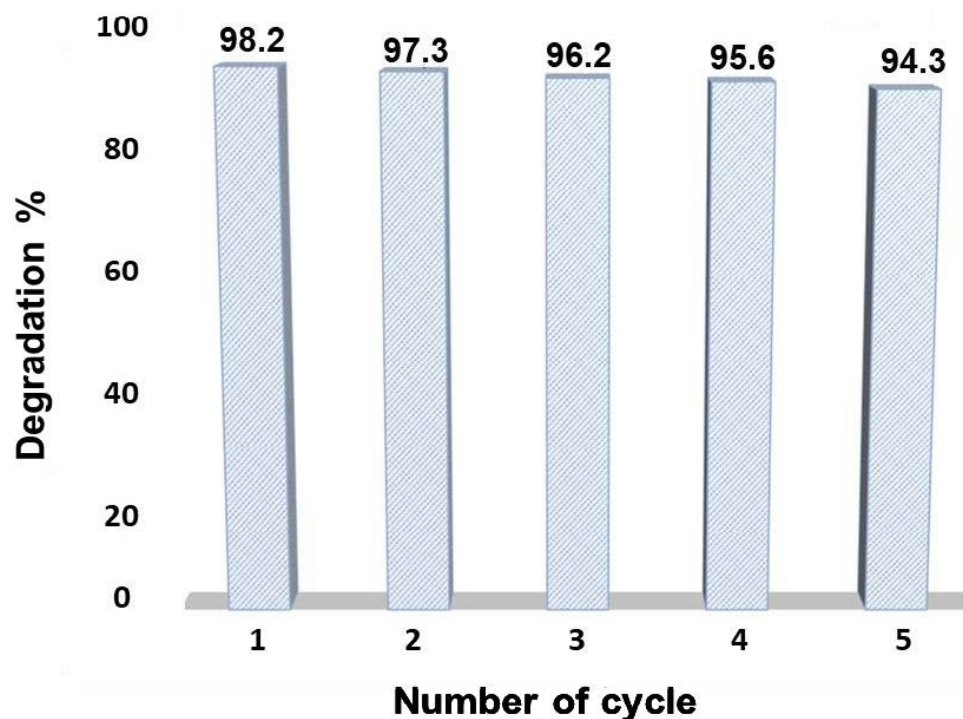


**Figure 13.** Reusability of the prepared TiO<sub>2</sub> NPs for the degradation of Remazol Brilliant Red F3B (Reactive Red 180).

#### 4. Conclusions

Titanium ions were successfully reduced into titanium dioxide nanoparticles using an innovative aqueous biological extract acquired from *Aloe vera* leaves. The calcination time was changed while maintaining a constant temperature of 500 °C. This allowed us to obtain nanoparticles with various structural, morphological, optical and photocatalytic properties. As the calcination time was increased, the nanoparticle size was reduced. Similarly, small diameter nanoparticles had new optical properties which required an improvement of the material's photocatalytic activity. TiO<sub>2</sub> nanoparticles were used to remove RR180 from aqueous solutions. Their photodegradation capacity (100%) under visible light irradiation toward dye RR180 varied with time, from 1 h with TiO<sub>2</sub> nanopowders (D1; size 23 ± 2 nm) to 2 h with TiO<sub>2</sub> NPs (D2; 83 ± 5 nm).

**Author Contributions:** Z.A. was responsible for practically conducting the research, data collection and analysis. M.S. provided the intellectual input, and designed and approved the protocols to be followed in the study. All authors have read and agreed to the published version of the manuscript.

**Funding:** Shaqra University, grant number IFP2021-006 to Zahrah Alhalili. The authors extend their appreciation to the Deputyship for Research and Innovation, Ministry of Education in Saudi Arabia for funding this research work through the project number (IFP2021-006).

**Data Availability Statement:** All data generated or analyzed during this study are included in this published article.

**Conflicts of Interest:** The authors declare no conflict of interest.

## References

1. Singh, R.L.; Singh, P.K.; Singh, R.P. Enzymatic decolorization and degradation of azo dyes. *Int. Biodeterior. Biodeg.* **2015**, *104*, 21. [CrossRef]
2. Selvaraj, V.; Karthika, T.S.; Mansiya, C.; Alagar, M. An over review on recently developed techniques, mechanisms and intermediate involved in the advanced azo dye degradation for industrial applications. *J. Mol. Struct.* **2021**, *1224*, 129195. [CrossRef]
3. Calenciuc, C.; Fdez-Sanromán, A.; Lama, G.; Annamalai, S.; Sanromán, A.; Pazos, M. Recent Developments in Advanced Oxidation Processes for Organics-Polluted Soil Reclamation. *Catalysts* **2022**, *12*, 64. [CrossRef]
4. Kiendrebeogo, M.; Karimi Estahbanati, M.R.; Ouarda, Y.; Drogui, P.; Tyagi, R.D. Electrochemical degradation of nanoplastics in water: Analysis of the role of reactive oxygen species. *Sci. Total Environ.* **2022**, *808*, 151897. [CrossRef] [PubMed]
5. Tsarev, S.; Collins, R.N.; Ilton, E.S.; Fahy, A.; Waite, T.D. The short-term reduction of uranium by nanoscale zero-valent iron (nZVI): Role of oxide shell, reduction mechanism and the formation of U(v)-carbonate phases. *Environ. Sci. Nano* **2017**, *4*, 1304. [CrossRef]
6. Dey, A.S.; Bose, H.; Mohapatra, B.; Sar, P. Biodegradation of Unpretreated Low-Density Polyethylene (LDPE) by *Stenotrophomonas* sp. and *Achromobacter* sp., Isolated from Waste Dumpsite and Drilling Fluid. *Front. Microbiol.* **2020**, *11*, 603210. [CrossRef] [PubMed]
7. Okonji, S.O.; Yu, L.; Dominic, J.A.; Pernitsky, D.; Achari, G. Adsorption by Granular Activated Carbon and Nano Zerovalent Iron from Wastewater: A Study on Removal of Selenomethionine and Selenocysteine. *Water* **2021**, *13*, 23. [CrossRef]
8. Xu, M.; Wu, C.; Zhou, Y. Advancements in the Fenton Process for Wastewater Treatment. In *Advanced Oxidation Processes—Applications, Trends, and Prospects*; IntechOpen: London, UK, 2020; Volume 90256, p. 182.
9. Palanisamy, S.; Nachimuthu, P.; Awasthi, M.K.; Ravindran, B.; Chang, S.W.; Palanichamy, M.; Nguyen, D.D. Application of electrochemical treatment for the removal of triazine dye using aluminium electrodes. *J. Water Supply Res. Technol.* **2020**, *69*, 345–354. [CrossRef]
10. Franca, R.; Oliveira, M.C.; Pinheiro, H.M.; Lourenço, N.D. Biodegradation products of a sulfonated azo dye in aerobic granular sludge sequencing batch reactors treating a simulated textile wastewater. *ACS Sustain. Chem. Eng.* **2019**, *7*, 14697. [CrossRef]
11. Zhang, S.; Zhong, L.; Wang, J.; Tang, A.; Yang, H. Coated clay presenting super high adsorption capacity for Congo Red. *Chem. Eng. J.* **2021**, *406*, 126784. [CrossRef]
12. Li, H.; Meng, R.; Guo, Y.; Chen, B.; Jiao, Y.; Ye, C.; Long, Y.; Tadich, A.; Yang, Q.-H.; Jaroniec, M.; et al. Reversible electrochemical oxidation of sulfur in ionic liquid for high-voltage Al–S batteries. *Nat. Commun.* **2021**, *12*, 5714. [CrossRef] [PubMed]
13. Ibrahim, M.I.; Awad, M.; Al-Farraj, A.S.; Al-Turki, A.M. Stability and Dynamic Aggregation of Bare and Stabilized Zero-Valent Iron Nanoparticles under Variable Solution Chemistry. *Nanomaterials* **2020**, *10*, 192. [CrossRef]
14. Rahman, Z.; Singh, V.P. The relative impact of toxic heavy metals (THMs) (arsenic (As), cadmium (Cd), chromium (Cr)(VI), mercury (Hg), and lead (Pb)) on the total environment. *Environ. Monit. Assess.* **2019**, *191*, 419. [CrossRef] [PubMed]
15. Ma, X.; Li, S.; Hou, Y.; Lv, H.; Li, J.; Cheng, T.; Yang, L.; Wu, H. Adsorption of low-concentration organic pollutants from typical coal-fired power plants by activated carbon injection. *Process Saf. Environ. Prot.* **2022**, *159*, 1174. [CrossRef]
16. Nagaraj, G.; Dhayal Raj, A.; Irudayaraj, A.A.; Josephine, R. Tuning the Optical Band Gap of Pure TiO<sub>2</sub> via Photon Induced Method. *Optik* **2018**, *179*, 889–894.
17. Wang, S.; Ding, Z.; Chang, X.; Xu, J. Modified Nano-TiO<sub>2</sub> Based Composites for Environmental Photocatalytic Applications. *Catalysts* **2020**, *10*, 759. [CrossRef]
18. Jang, H.D.; Kim, S.-K.; Kim, S.-J. Effect of Particle Size and Phase Composition of titanium Dioxide Nanoparticles on the Photocatalytic Properties. *J. Nanopart. Res.* **2001**, *3*, 141. [CrossRef]
19. Hao, W.C.; Zheng, S.K.; Wang, T.M. Comparison of the photocatalytic activity of TiO<sub>2</sub> powder. *J. Mater. Sci. Lett.* **2002**, *21*, 1627. [CrossRef]
20. Maira, A.J.; Yeung, K.L.; Lee, C.Y.; Yue, P.L.; Chan, C.K. Size Effects in Gas-Phase Photo-oxidation of Trichloroethylene Using Nanometer-Sized TiO<sub>2</sub> Catalysts. *J. Catal.* **2000**, *196*, 185. [CrossRef]
21. Krýsa, J.; Keppert, M.; Štengl, V.; Šubrt, J. The effect of thermal treatment on the properties of TiO<sub>2</sub> photocatalyst. *Mater. Chem. Phys.* **2004**, *86*, 333. [CrossRef]
22. Ropers, M.-H.; Terrisse, H.; Mercier-Bonin, M.; Humbert, B. Titanium Dioxide as Food Additive. In *Application of Titanium Dioxide*; InTech: Rijeka, Croatia, 2017.
23. Nabi, G.; Raza, W.; Tahir, M.B. Green Synthesis of TiO<sub>2</sub> Nanoparticle Using Cinnamon Powder Extract and the Study of Optical Properties. *J. Inorg. Org. Pol. Mat.* **2020**, *30*, 1425. [CrossRef]
24. Diriba, T.F.; Deresa, E.M. Botanical description, ethnomedicinal uses, phytochemistry, and pharmacological activities of genus Kniphofia and Aloe. *Arab. J. Chem.* **2022**, *15*, 9.
25. Zhong, X.; Yang, B.; Zhang, X.; Jia, J.; Yi, G. Effect of calcining temperature and time on the characteristics of Sb-doped SnO<sub>2</sub> nanoparticles synthesized by the sol-gel method. *Particuology* **2012**, *10*, 365. [CrossRef]
26. Lai, C.; An, Z.; Yi, H.; Huo, X.; Qin, L.; Liu, X.; Li, B.; Zhang, M.; Liu, S.; Li, L.; et al. Enhanced visible-light-driven photocatalytic activity of bismuth oxide via the decoration of titanium carbide quantum dots. *J. Coll. Inter. Sci.* **2021**, *600*, 161. [CrossRef] [PubMed]

27. Li, B.; Lai, C.; Zhang, M.; Liu, S.; Yi, H.; Liu, X.; An, N.; Zhou, X.; Li, L.; Fu, Y.; et al. N, S-GQDs and Au nanoparticles co-modified ultrathin Bi<sub>2</sub>MoO<sub>6</sub> nanosheet with enhanced charge transport dynamics for full-spectrum-light-driven molecular oxygen activation. *Chem. Eng. J.* **2021**, *409*, 128281. [[CrossRef](#)]
28. Senthilkumar, S.; Ashok, M.; Kashinath, L.; Sanjeeviraja, C.; Rajendran, A. Phytosynthesis and characterization of TiO<sub>2</sub> nanoparticles using diospyros ebenum leaf extract and their antibacterial and photocatalytic degradation of crystal violet. *Smart Sci.* **2017**, *6*, 1–9. [[CrossRef](#)]
29. Verma, V.; Al-Dossari, M.; Singh, J.; Rawat, M.; Kordy, M.G.M.; Shaban, M. A Review on Green Synthesis of TiO<sub>2</sub> NPs: Synthesis and Applications in Photocatalysis and Antimicrobial. *Polymers* **2022**, *14*, 1444. [[CrossRef](#)]
30. Alhalili, Z.; Romdhani, C.; Chemingui, H.; Smiri, M. Removal of dithietherthiol (DTT) from water by membranes of cellulose acetate (AC) and AC doped ZnO and TiO<sub>2</sub> nanoparticles. *J. Saudi Chem. Soc.* **2021**, *25*, 8. [[CrossRef](#)]
31. Alhalili, Z.; Romdhani, C.; Elarbaoui, S.; Smiri, M. Identification and removal of sulfhydryl groups from wastewaters. *J. Saudi Chem. Soc.* **2021**, *25*, 11. [[CrossRef](#)]
32. Alhalili, Z.; Souli, H.; Smiri, M. Effect of LEO (Lycium Essential Oils) as green inhibitors of calcium carbonate scale on nanoparticles-doped ultrafiltration membrane (UFM) and water treatment. *Arab. J. Sci. Eng.* **2022**, *47*, 6233. [[CrossRef](#)]
33. Pokrajac, L.; Abbas, A.; Chrzanowski, W.; Dias, G.M.; Eggleton, B.J.; Maguire, S.; Maine, E.; Malloy, T.; Nathwani, J.; Nazar, L.; et al. Nanotechnology for a Sustainable Future: Addressing Global Challenges with the International Network4Sustainable Nanotechnology. *ACS Nano* **2021**, *15*, 12. [[CrossRef](#)] [[PubMed](#)]
34. Alhalili, Z. Green synthesis of copper oxide nanoparticles CuO NPs from *Eucalyptus Globoulus* leaf extract: Adsorption and design of experiments. *Arab. J. Chem.* **2022**, *15*, 103739. [[CrossRef](#)]
35. Jain, A.; Vaya, D. Photocatalytic activity of TiO<sub>2</sub> nanomaterial. *J. Chil. Chem. Soc.* **2017**, *62*, 3683–3690. [[CrossRef](#)]
36. Aphairaj, D.; Wirunmongkol, T.; Pavasupree, S.; Limsuwan, P. Effect of calcination temperatures on structures of TiO<sub>2</sub> powders prepared by hydrothermal method using thai leucoxene mineral. *Energy Procedia* **2011**, *9*, 539–544. [[CrossRef](#)]
37. Indrayana, I.P.T.; Tjuana, L.A.; Tuny, M.T.; Kurnia. Nanostructure and optical properties of Fe<sub>3</sub>O<sub>4</sub>: Effect of calcination temperature and dwelling time. *J. Phys. Conf. Ser.* **2019**, *1341*, 082044. [[CrossRef](#)]
38. Xing, S.; Song, S.; Xiang, J. Low temperature combustion synthesis and photoluminescence mechanism of ZnO/ZnAl<sub>2</sub>O<sub>4</sub> composite phosphors. *Opt. Int. J. Light Electron. Opt.* **2020**, *208*, 164526. [[CrossRef](#)]
39. Zhao, Y.; Li, C.; Liu, X.; Gu, F.; Jiang, H.; Shao, W.; Zhang, L.; He, Y. Synthesis and optical properties of TiO<sub>2</sub> nanoparticles. *Mater. Lett.* **2007**, *61*, 79. [[CrossRef](#)]
40. Asahi, R.; Morikawa, T.; Ohwaki, T.; Aoki, K.; Taga, Y. Visible-light photocatalysis in nitrogen-doped titanium oxides. *Science* **2001**, *293*, 269. [[CrossRef](#)]
41. Massima Mouele, E.S.; Dinu, M.; Cummings, F.; Fatoba, O.O.; Zar Myint, M.T.; Kyaw, H.H.; Parau, A.C.; Vladescu, A.; Francesconi, M.G.; Pescetelli, S.; et al. Effect of Calcination Time on the Physicochemical Properties and Photocatalytic Performance of Carbon and Nitrogen Co-Doped TiO<sub>2</sub> Nanoparticles. *Catalysts* **2020**, *10*, 847. [[CrossRef](#)]
42. Salah, N.H. Etude de la dégradation photocatalytique de polluants organiques en présence de dioxyde de titane, en suspension aqueuse et en lit fixe. Ph.D. Thesis, Université de Grenoble, Grenoble, France, Université Mentouri, Constantine, Algeria, 2012; 175p.
43. Zhang, Y.; Miao, B.; Chen, Q.; Bai, Z.; Cao, Y.; Davaa, B. Synthesis, structure, and photocatalytic activity of TiO<sub>2</sub>-montmorillonite composites. *Catalysts* **2022**, *12*, 486. [[CrossRef](#)]
44. Bao, Z.; Wang, S.; Yu, X.; Gao, Y.; Wen, Z. In Situ Synthesis and Photocatalytic Properties of Titanium Dioxide Nanoparticles on Cotton Fabrics. *Water Air Soil Pollut.* **2019**, *230*, 169. [[CrossRef](#)]
45. Wahi, R.K.; Yu, W.W.; Liu, Y.; Mejia, M.L.; Falkner, J.C.; Nolte, W.; Colvin, V.L. Photodegradation of Congo Red catalyzed by nanosized TiO<sub>2</sub>. *J. Mol. Catal. A Chem.* **2005**, *242*, 48. [[CrossRef](#)]
46. Bilal, M.; Umar, M.; Bakhsh, E.M.; Ali, J.; Ahmad, R.; Akhtar, K.; Khan, S.B. Structural, optical and photocatalytic properties of silver-doped magnesia: Computational and experimental study. *J. Mol. Liq.* **2021**, *339*, 117176. [[CrossRef](#)]
47. Uribe-López, M.C.; Heidalgo-lópez, M.C.; López-gonzález, R.; Frías-márquez, D.M.; Núñez-Nogueira, G.; Hernández-Castillo, D.; Alvarez-Lemus, M.A. Photocatalytic activity of ZnO nanoparticles and the role of the synthesis method on their physical and chemical properties. *J. Photochem. Photobiol. A Chem.* **2021**, *404*, 112866. [[CrossRef](#)]
48. Jawed, A.; Verma, R.; Saxena, V.; Pandey, L.M. Photocatalytic metal nanoparticles: A green approach for degradation of dyes. In *Photocatalytic Degradation of Dyes*; Elsevier: Amsterdam, The Netherlands, 2021; pp. 251–275.
49. Lee, S.Y.; Kang, D.; Jeong, S.; Do, H.T.; Kim, J.H. Photocatalytic Degradation of Rhodamine B Dye by TiO<sub>2</sub> and Gold Nanoparticles Supported on a Floating Porous Polydimethylsiloxane Sponge under Ultraviolet and Visible Light Irradiation. *ACS Omega* **2020**, *5*, 4233. [[CrossRef](#)]
50. Slama, H.B.; Bouket, A.C.; Pourhassan, Z.; Alenezi, F.N.; Silini, A. Applied sciences diversity of synthetic dyes from textile industries, discharge impacts and treatment methods. *Appl. Sci.* **2021**, *11*, 6255. [[CrossRef](#)]
51. Vorontsov, A.V.; Kabachkov, E.N.; Balikhin, I.L.; Kurkin, E.N.; Troitskii, V.N.; Smirniotis, P.G. Correlation of surface area with photocatalytic activity of TiO<sub>2</sub>. *J. Adv. Oxi. Tech.* **2018**, *21*, 127. [[CrossRef](#)]
52. Li, D.; Song, H.; Meng, X.; Shen, T.; Sun, J.; Han, W.; Wang, X. Effects of Particle Size on the Structure and Photocatalytic Performance by Alkali-Treated TiO<sub>2</sub>. *Nanomaterials* **2020**, *10*, 546. [[CrossRef](#)]

53. Venkatesh, K.S.; Krishnamoorthi, S.R.; Palani, N.S.; Thirumal, V.; Jose, S.P.; Wang, F.-M.; Ilangovan, R. Facile one step synthesis of novel TiO<sub>2</sub> nanocoral by sol–gel method using *Aloe vera* plant extract. *Indian J. Phys.* **2015**, *89*, 445. [[CrossRef](#)]
54. Li, L.; Yan, J.; Wang, T.; Zhao, Z.-J.; Zhang, J.; Gong, J.; Guan, N. Sub-10 nm rutile titanium dioxide nanoparticles for efficient visible-light-driven photocatalytic hydrogen production. *Nat. Commun.* **2015**, *6*, 1–10. [[CrossRef](#)]
55. Kang, C.W.; Kolya, H. Green synthesis of Ag-Au bimetallic nanocomposites using waste tea leaves extract for degradation congo red and 4-Nitrophenol. *Sustainability* **2021**, *13*, 3318. [[CrossRef](#)]
56. Geun, C.P.; Tae, Y.S.; Chae, H.P.; Jun, H.L.; Jinho, J. Effects of Calcination Temperature on Morphology, Microstructure, and Photocatalytic Performance of TiO<sub>2</sub> Mesocrystals. *Ind. Eng. Chem. Res.* **2017**, *56*, 8235–8240.